Composition and density of nanoscale calcium–silicate–hydrate in cement

ANDREW J. ALLEN[1]*, JEFFREY J. THOMAS[2] AND HAMLIN M. JENNINGS[2,3]

[1]Ceramics Division, National Institute of Standards and Technology, Gaithersburg, Maryland 20899, USA
[2]Department of Civil and Environmental Engineering, Northwestern University, Evanston, Illinois 60208, USA
[3]Department of Materials Science and Engineering, Northwestern University, Evanston, Illinois 60208, USA
*e-mail: andrew.allen@nist.gov

Published online: 25 March 2007; doi:10.1038/nmat1871

Although Portland cement concrete is the world's most widely used manufactured material, basic questions persist regarding its internal structure and water content, and their effect on concrete behaviour. Here, for the first time without recourse to drying methods, we measure the composition and solid density of the principal binding reaction product of cement hydration, calcium–silicate–hydrate (C–S–H) gel, one of the most complex of all gels. We also quantify a nanoscale calcium hydroxide phase that coexists with C–S–H gel. By combining small-angle neutron and X-ray scattering data, and by exploiting the hydrogen/deuterium neutron isotope effect both in water and methanol, we determine the mean formula and mass density of the nanoscale C–S–H gel particles in hydrating cement. We show that the formula, $(CaO)_{1.7}(SiO_2)(H_2O)_{1.80}$, and density, 2.604 Mg m^{-3}, differ from previous values for C–S–H gel, associated with specific drying conditions. Whereas previous studies have classified water within C–S–H gel by how tightly it is bound, in this study we classify water by its location—with implications for defining the chemically active (C–S–H) surface area within cement, and for predicting concrete properties.

With more than 11 billion metric tons consumed each year, Portland cement concrete is the world's most widely used manufactured material, but is also one of the most complex. After more than a century of study[1], basic questions persist regarding its internal structure over the nanometre to macroscopic scale range and its effects on concrete behaviour. Most of these questions pertain to the primary hydration product and binding phase of Portland cement paste, the calcium silicate hydrate (C–S–H) gel. When cement and water are mixed, this phase precipitates as clusters of nanoscale colloidal particles with an associated internal pore system[2]. The complex behaviour of concrete is largely related to the viscoelastic response of C–S–H gel to mechanical loading (creep) and to relative humidity changes (drying shrinkage)[3,4]—both critically affecting concrete performance and the subject of increasingly sophisticated modelling efforts[5,6] that demand an increased understanding of C–S–H gel at the nanoscale level.

In this context, knowledge of the mean composition and density of the solid C–S–H component, together with its microstructure over a scale range from nanometres to several micrometres, is essential. Neutron and X-ray scattering can provide such characterization, and this paper reports the results of a unique series of scattering experiments that, for the first time, precisely determine the composition and mass density of the solid nanoscale C–S–H particles. These results define the chemically active surface area in cement and help resolve an important and long-standing issue regarding the distribution of water within the nanostructure of C–S–H. Saturated C–S–H gel has the approximate formula $(CaO)_{1.7}SiO_2(H_2O)_4$, including liquid water between the particles[2]. Removal of liquid water by equilibrating to 11% relative humidity (RH) leaves some adsorbed water on the C–S–H particle surfaces and lowers the H_2O/SiO_2 ratio to about 2.1. Stronger drying in vacuum (D-drying), or by heating to 105 °C, removes some water physically bound within the colloidal C–S–H particles, resulting in a lower H_2O/SiO_2 ratio of about 1.4. The results reported here, which do not rely on drying or desorption, establish the H_2O/SiO_2 ratio for solid C–S–H that includes all water physically bound within the internal structure of the particles, but no adsorbed or liquid water outside the particle boundaries.

Although techniques such as transmission electron microscopy and nuclear magnetic resonance greatly elucidate the nature of C–S–H gel[7–10], they have yet to link composition, density and morphology into a single comprehensive picture. Previous small-angle X-ray[11–18] and neutron[19–34] scattering (SAXS and SANS) studies have characterized the C–S–H gel morphology and, using the H_2O/D_2O SANS contrast variation method, have selected a solid C–S–H formula/density scenario from postulated models[35]. However, the ready exchange of the hydrogen in C–S–H for the deuterium in D_2O precludes an unambiguous determination of the absolute scattering contrast between solid C–S–H and the pore water. The presence of nanoscale $Ca(OH)_2$, coexisting with the gel, further obstructs a simple determination of the C–S–H contrast match point[34,36]. Here, CH_3OH/CD_3OH methanol SANS contrast variation data, where deuterium does not exchange with the hydrogen in C–S–H, are compared both with water SANS contrast variation data and with absolute-calibrated SAXS data. (SAXS and SANS give different scattered intensities.) From this comparison, the nanoscale $Ca(OH)_2$ phase is quantified and the solid C–S–H formula, $(CaO)_x(SiO_2)(H_2O)_y$, is determined in terms of x and y, together with its mass density.

Our approach can be summarized with reference to Fig. 1, which illustrates schematically our picture of the nanoscale C–S–H phase that forms between cement clinker grains and binds them together, on the basis of previous work[17,22,25,30,31]. The objective is to determine the composition and density of the solid particles

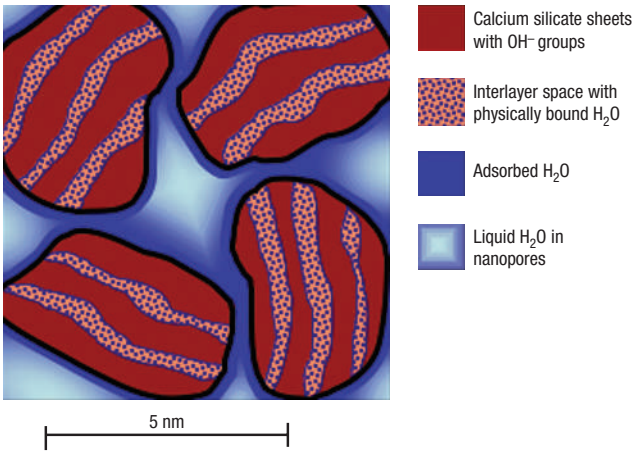

Figure 1 Schematic diagram of the nanoscale C–S–H particles. The black lines indicate the small-angle scattering interface between solid C–S–H and liquid water. The composition and density of the latter are determined in the present experiments by SANS contrast variation and SAXS/SANS contrast comparison. The particle-size scale bar, although not critical to the present discussion, is derived from previous SANS studies by the authors[17,22,25,30,31]. With solid C–S–H in the form of nanometre-scale particles, the water content in the solid is lower, and the density higher, than would be found in tobermorite or jennite minerals (frequently discussed in relation to C–S–H gel[2,7,36,41]) with structures based on infinite sheets separated by layers of physically bound water. This is because there is a non-negligible proportion of Ca–Si layers that are exposed at a particle surface and thus do not contain physically bound water. SANS and SAXS measure structure over the scale range from nanometres to micrometres, and the contrast is affected by the composition and density of the particles, but they are not sensitive to the internal particle structure at the sub-nanometre level. The nanoscale $Ca(OH)_2$ is not shown, but is distinct from the C–S–H particles and is probably slightly coarser—see Supplementary Information.

(within the black lines) as seen by SANS or SAXS. Previous work[17] indicates that this perimeter defines the chemically active surface area in hydrating cement. Our results rely on SANS and SAXS measurements of the scattering probability per unit of sample volume, known as the absolute-calibrated small-angle scattered intensity, $I(Q)$, measured over several decades of the scattering vector magnitude, Q, where $Q = (4\pi/\lambda)\sin(\phi_S/2)$, λ is the incident wavelength and ϕ_S is the scattering angle[37]. $I(Q)$ is effectively a Fourier transform of the internal solid/void microstructure, with coarse (fine) features associated with low (high) Q. The significant flat-background scattering must be subtracted out. In what follows, one-standard-deviation uncertainties are indicated either by scatter in the data or by vertical bars plotted at each data point. Other numerical results are presented with one-standard-deviation uncertainties in parentheses, in least significant digits.

The different effects of isotope exchange on the absolute-calibrated SANS data for ordinary Portland cement (OPC) paste in water (H_2O/D_2O) and in d_3-methanol (CH_3OH/CD_3OH) are shown in Fig. 2a,b. The intensity variation follows the scattering contrast between solid and pore liquid and, in the nanoscale regime (high Q), gives the parabolic contrast curves in Fig. 2c that show the scattering contrast is reduced for full deuteration. At coarse length scales (low Q), the scattered intensity curves for OPC in H_2O and D_2O cross (Fig. 2a) owing to the different exchange properties of the mainly nanoscale C–S–H (all hydrogen exchanges to form C–S–D) and the mainly micrometre-scale $Ca(OH)_2$ (no exchange—see Fig. 2d). The curves for OPC in CH_3OH and CD_3OH (Fig. 2b) do not cross, because neither C–S–H nor $Ca(OH)_2$ exchanges hydrogen with the methyl (CH_3/CD_3) group.

Figure 2c shows H_2O/D_2O SANS contrast curves for the regime $Q > 1\,nm^{-1}$, where the scattering is dominated by the nanoscale C–S–H/pore interface. The parabolic shape arises because the contrast is proportional to the squared difference in neutron scattering-length density between the solid phase and the pore fluid, which varies linearly with deuterium content. (The neutron scattering length, which can be negative, is the intrinsic scattering strength per atom, and can be obtained from published tables[38].) The intensity should go to zero at the match point where the solid scattering-length density, ρ, matches the H_2O/D_2O value, interpolated between $\rho_{H_2O} = -0.561$ and $\rho_{D_2O} = +6.402$, each $\times 10^{14}\,m^{-2}$. The non-zero contrast minima (Fig. 2c) are evidence for at least two distinct nanoscale phases with different contrast match points.

The calculated contrast curve for $Ca(OH)_2$ ($\rho_{CH} = +1.643 \times 10^{14}\,m^{-2}$) in H_2O/D_2O is different (Fig. 2d) from the measured curves shown. It has an increased contrast with D_2O, suggesting that micrometre-scale $Ca(OH)_2$, which dominates the scattering at low Q, is associated with the crossover in Fig. 2a. At high Q, the measured contrast curves (Fig. 2c) can each be fitted with two component parabolas[34]: one for $Ca(OH)_2$ with a 31% (molar) D_2O match point, and the other for C–S–H constrained only by requiring zero intensity at contrast match. A consistent C–S–H contrast parabola is obtained with 81(1)% D_2O contrast match, together with a $Ca(OH)_2$ component that contributes a small fraction, f_{CH}, to the scattered intensity in H_2O (Fig. 2c). The C–S–H scattering-length density, ρ_{CSH}, is not determined as C–S–H exchanges with H_2O/D_2O to form C–S–D, and the C–S–H composition, mass density and volume fraction remain unknown. We seek, experimentally, the neutron scattering-length densities, ρ_{CSH}, and ρ_{CSD} for C–S–D, and the X-ray scattering-length density, ρX_{CSH}, for C–S–H, because they provide the quantitative constraints needed to determine the solid C–S–H x and y composition parameters and its mass density.

Having quantified the nanoscale $Ca(OH)_2$ component by H_2O/D_2O SANS contrast variation, methanol CH_3OH/CD_3OH SANS contrast studies can provide a measure of ρ_{CSH}. Although exchanging water for methanol shuts down the cement hydration reactions, the SANS data shown in Fig. 3 indicate that the hydrated microstructure is not otherwise disturbed: the data for OPC in H_2O and in CH_3OH do not deviate from each other throughout the measured Q range—a defining characteristic for identical scattering microstructures, here over the nanometre-to-micrometre scale range. However, as the OH exchange between d_3-methanol (CD_3OH) and C–S–H does not form C–S–D, the contrast curve for $Ca(OH)_2$ in CH_3OH/CD_3OH ($\rho_{CH_3OH} = -0.373$, $\rho_{CD_3OH} = +4.276$, each $\times 10^{14}\,m^{-2}$, contrast match at 42.4% CD_3OH from Fig. 2d) has less effect on the measured cement contrast curves in methanol (contrast minima at ≈63% CD_3OH) than in water.

Because clustering of CH_3 and CD_3 methyl groups[39] within the fluid mixture gives significant scattering around the CH_3OH/CD_3OH contrast match point with C–S–H, the methanol contrast data are analysed by comparing the cement scattered intensity in CH_3OH with that in CD_3OH. Figure 4 shows the point-by-point deduced scattering-length density of the solid phase, ρ_{solid}, versus Q for both OPC and tricalcium silicate (denoted C_3S, the main cement mineral often used as a model system for OPC). Each ρ_{solid} value, derived as indicated in Fig. 4, is a mix of ρ_{CSH} and the smaller ρ_{CH}. It increases with Q owing to a decreasing $Ca(OH)_2$ contribution with decreasing length scale, down to the nanoscale regime indicated by the box. Within the box, both cements give statistically constant ρ_{solid} values

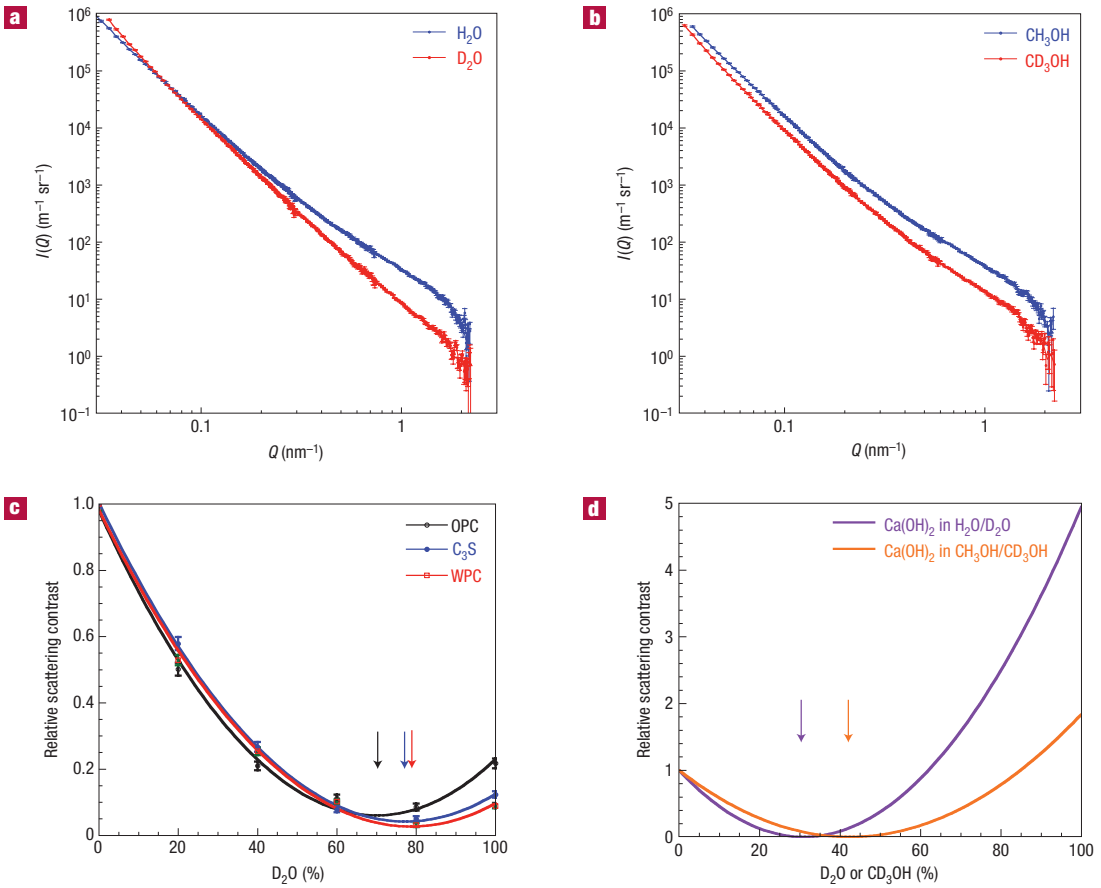

Figure 2 Effect of isotope exchange on absolute-calibrated SANS data. a, Experimental SANS absolute-calibrated $I(Q)$ data versus Q for an OPC coupon, 0.4 water-to-cement (w/c) mass ratio, hydrated for 28 d at 20 °C, immersed in H_2O, and for a coupon where H_2O has been exchanged for D_2O. **b**, As in **a**, but for a coupon with the H_2O exchanged for CH_3OH methanol and where CH_3OH has been further exchanged for CD_3OH. **c**, Relative SANS intensity (scattering contrast) data in the nanoscale regime ($Q > 1.0$ nm^{-1}) versus molar D_2O content, together with two-component parabola fits, for OPC, C_3S and WPC (white Portland cement with 18% mass silica fume added) after 28 d hydration in H_2O. (C = CaO, S = SiO_2). The arrows indicate D_2O molar fractions at the scattering contrast minima. The fitted parabolas give $Ca(OH)_2$ contributions to the scattered intensity in H_2O, f_{CH}, for OPC: 0.034(5), C_3S: 0.019(5) and WPC: 0.011(5). **d**, Calculated relative scattering contrast curves for $Ca(OH)_2$: SANS intensity versus deuterated molar fraction for both H_2O/D_2O and CH_3OH/CD_3OH pore fluid exchange.

with means of 2.544(4) for OPC and 2.560(5) for C_3S, each $\times 10^{14}$ m^{-2}. To deduce ρ_{CSH}, the measured ρ_{solid} are corrected using the known ρ_{CH} and fitted fraction, f_{CH}, of the SANS intensity attributed to nanoscale $Ca(OH)_2$ in H_2O. Specifically, $\rho_{CSH} = \rho_{H_2O} + \{[(\rho_{solid} - \rho_{H_2O})^2 - f_{CH}(\rho_{CH} - \rho_{H_2O})^2]/(1 - f_{CH})\}^{0.5}$, giving for OPC and C_3S, respectively, $\rho_{CSH} = 2.572(5)$ and 2.576(6), each $\times 10^{14}$ m^{-2}, or an average: $\rho_{CSH} = 2.574(5) \times 10^{14}$ m^{-2}.

With a known ρ_{CSH}, we return to the H_2O/D_2O SANS contrast component parabola for C–S–H with its fitted match point at 81(1)% D_2O. For C–S–H in D_2O, the solid phase exchanges with D_2O to give C–S–D. By using this information and scaling the unknown mass density and molecular weight in proportion to each other, we obtain the C–S–D neutron scattering-length density, $\rho_{CSD} = 5.667(48) \times 10^{14}$ m^{-2}, with the increased uncertainty arising from that in the fitted contrast match point.

To determine ρX_{CSH}, the SAXS and SANS scattered intensities are compared, correcting for the known $Ca(OH)_2$ component. The relevant X-ray scattering-length (form-factor) densities, denoted ρX_{CSH}, ρX_{CH}, ρX_{H_2O} and ρX_{CH_3OH}, are derived from their respective atomic electron densities using standard results[40]. Of these, ρX_{CSH} is the only unknown, but it can be deduced from the SAXS/SANS intensity ratio, I_{SAXS}/I_{SANS}, measured over the same (high) Q range for cement in either H_2O or CH_3OH. In H_2O:

$$\frac{I_{SAXS}}{I_{SANS}} = \frac{[(1-\alpha_{CH})(\rho X_{CSH} - \rho X_{H_2O})^2 + \alpha_{CH}(\rho X_{CH} - \rho X_{H_2O})^2]}{[(1-\alpha_{CH})(\rho_{CSH} - \rho_{H_2O})^2 + \alpha_{CH}(\rho_{CH} - \rho_{H_2O})^2]}, \quad (1)$$

where $\{\alpha_{CH}/(1 - \alpha_{CH})\} = \{f_{CH}/(1 - f_{CH})\}(\rho_{CSH} - \rho_{H_2O})^2/(\rho_{CH} - \rho_{H_2O})^2$, rescaling f_{CH} to correct for the different SANS contrasts of C–S–H and $Ca(OH)_2$ with H_2O. Figure 3 includes a comparison of ultrasmall-angle X-ray scattering (USAXS) data with SANS data for OPC in H_2O. The data are approximately parallel throughout the entire Q range, indicating that SAXS and SANS see essentially the same microstructure. At the highest Q values shown, the measured ratio, I_{SAXS}/I_{SANS}, for OPC is 17.8(8), and it is 16.7(7) for C_3S. Substitution of these values into equation (1) yields a mean result of $\rho X_{CSH} = 22.35(20) \times 10^{14}$ m^{-2}. An analogous equation applies for I_{SAXS}/I_{SANS} measured in CH_3OH. For OPC in CH_3OH (also in Fig. 3) the measured ratio is larger at 26.9(8), and it is 27.5(9) for C_3S. These give a mean result of $\rho X_{CSH} = 22.86(11) \times 10^{14}$ m^{-2}, almost in agreement with the H_2O

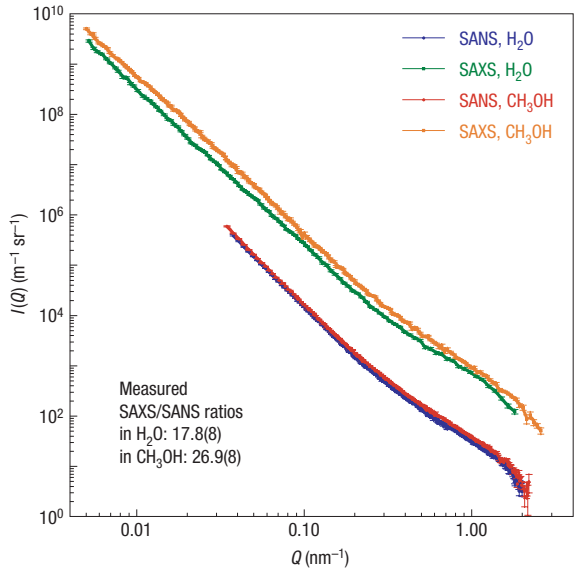

Figure 3 OPC SANS and SAXS intensity data in H_2O and CH_3OH on an absolute scale. Data versus Q for 0.4 w/c OPC coupons hydrated for 28 d at 20 °C in H_2O, and corresponding data for coupons hydrated similarly, then transferred to CH_3OH. The SANS data curves are almost identical throughout their Q range, indicating that the microstructure is not altered when the pore fluid is changed from water to methanol. Although subject to more scatter in the data, the SAXS curves in H_2O and CH_3OH are also parallel in these log–log plots throughout their Q range. These data extend to lower Q than SANS owing to use of the USAXS method (see the text). They confirm the unchanged microstructure following fluid exchange, although the increase in X-ray scattering contrast is apparent. The SANS and SAXS curves are approximately parallel to each other, particularly at high Q where the scattering is most closely associated with the nanoscale solid/pore interface, and where the SAXS/SANS intensity ratios, I_{SAXS}/I_{SANS}, are measured.

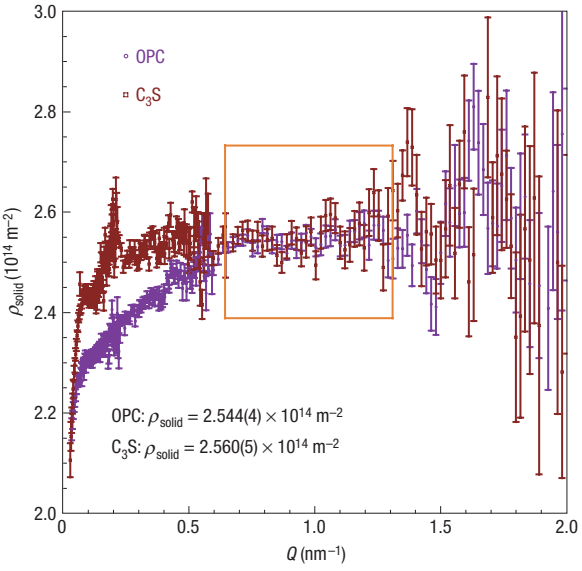

Figure 4 Neutron scattering-length density, ρ_{solid}, of nanoscale C–S–H/$Ca(OH)_2$ versus Q. For 0.4 w/c OPC and C_3S, hydrated for 28 d at 20 °C in H_2O, then transferred to methanol, the mean neutron scattering-length density of the solid, ρ_{solid}, is calculated from the ratio of the calibrated scattered intensities, I_{CH_3OH}/I_{CD_3OH}, measured (after flat-background subtraction) in 100% CH_3OH and 100% CD_3OH. For each Q, ρ_{solid} is given from the relation: $(\rho_{solid} - \rho_{CH_3OH})^2/(\rho_{solid} - \rho_{CD_3OH})^2 = I_{CH_3OH}/I_{CD_3OH}$, where ρ_{CH_3OH} and ρ_{CD_3OH} are the scattering-length densities of CH_3OH and CD_3OH. Computed values of ρ_{solid} are statistically constant for $Q > 0.55\,nm^{-1}$ for both OPC and C_3S, but become affected by background noise for $Q > 1.3\,nm^{-1}$; so only values within the box have been used.

result, although 2% larger. Some difficulty was encountered in achieving completely sealed specimens for the USAXS studies in CH_3OH, a problem that did not arise for any other measurement. Any loss of CH_3OH would elevate the I_{SAXS}/I_{SANS} ratio for the samples in CH_3OH, resulting in a correspondingly elevated value of ρX_{CSH}; so we exclude this result from what follows.

With ρ_{CSH}, ρ_{CSD} and ρX_{CSH} known, the composition parameters, x and y, and the mass density, may be derived from three simultaneous equations of the form[38,40]:

$$\rho_{CSH} = \frac{(x \cdot b_{CaO} + b_{SiO_2} + y \cdot b_{H_2O})}{(x \cdot M_{CaO} + M_{SiO_2} + y \cdot M_{H_2O})} N_A \times \text{mass density}, \qquad (2)$$

where b_{CaO}, and so on, are the neutron scattering lengths for CaO, SiO_2 and H_2O; M_{CaO}, and so on, are the corresponding molecular masses and N_A is Avogadro's number. Analogous equations can be written for ρ_{CSD} and ρX_{CSH}. Solving these equations for $(CaO)_x(SiO_2)(H_2O)_y$ yields $x = 1.85(27)$, $y = 1.87(15)$, density $= 2.605(24)\,Mg\,m^{-3}$, with all three experimental uncertainties correlated positively with each other. Experimental uncertainty in ρX_{CSH} and insensitivity of both SANS and SAXS to the Ca/Si ratio, x, are the main causes of the uncertainty. However, owing to the H_2O/D_2O sensitivity of SANS, the mass density is obtained to a fractional uncertainty <1% and the H_2O mass fraction in the solid C–S–H formula, $yM_{H_2O}/(xM_{CaO} + M_{SiO_2} + yM_{H_2O})$, can be deduced to comparable precision: 0.171(4). Whereas recent transmission electron microscopy work[36] suggests that the Ca/Si ratio may be as high as 1.85, even for C–S–H gel that is free of nanoscale $Ca(OH)_2$, most studies[2,34,41] indicate $Ca/Si \approx 1.7$ (a value within the above uncertainty range) for C–S–H in hydrated OPC and similar cements. Substituting $x = 1.70$ into the simultaneous equation (2), we obtain mean values of $y = 1.80(3)$, mass density $= 2.604(22)\,Mg\,m^{-3}$ and H_2O mass fraction $= 0.174(4)$.

Although the C–S–H solid/pore interface dominates the interfacial surface area within hydrated cement, our SANS experiments have revealed that nanoscale $Ca(OH)_2$ can contribute a small but significant fraction, α_{CH}, to the overall surface area. From f_{CH}, we obtain $\alpha_{CH} = 0.066(10)$ for OPC, 0.038(10) for C_3S and 0.022(10) for the white Portland cement system shown in Fig. 2c (that is, $\alpha_{CH} \approx 2f_{CH}$). SANS contrast variation can distinguish the C–S–H and $Ca(OH)_2$ structure over the full scale range. By combining SANS and ultrasmall-angle neutron scattering (USANS) data for OPC in water, measured at 80% and 32% D_2O (close to the C–S–H and $Ca(OH)_2$ contrast match points), the morphology of the non-matched component can be quantified over a scale range from ≈1 nm to ≈10 μm. Figure 5 shows how the C–S–H and $Ca(OH)_2$ components can be distinguished and rescaled to reveal their scattering contributions for OPC in H_2O. The fitted curves are based on a previously developed fractal model[22,25,30,34]. This has been applied in the SANS Q range to characterize, separately, the microstructure for OPC, C–S–H and $Ca(OH)_2$—see Supplementary Information. The model results confirm that the volume-fractal nature of hydrated cement is mainly attributable to the C–S–H component. The derived $Ca(OH)_2$ contribution to the OPC nanoscale surface area

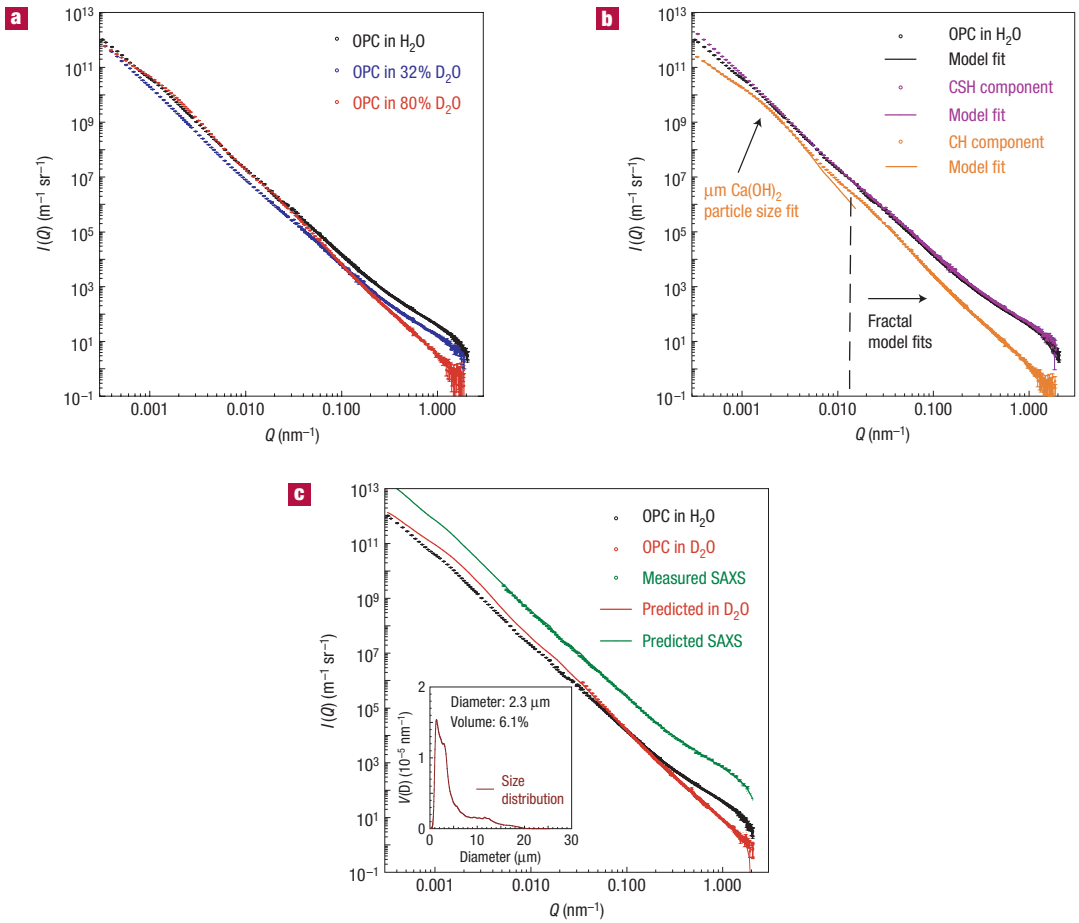

Figure 5 Combined SANS/USANS data showing C–S–H and $Ca(OH)_2$ components in OPC. a, SANS/USANS data for 0.4 w/c OPC in H_2O, in 32% molar D_2O ($Ca(OH)_2$ match) and in 80% molar D_2O (C–S–H match). For the latter two curves, the observed scattering is attributed to C–S–H and $Ca(OH)_2$, respectively. **b**, SANS/USANS data for the C–S–H and $Ca(OH)_2$ components rescaled to their predicted contrasts in H_2O; OPC data are shown again for comparison. The lines (see the Supplementary Information) represent fractal model fits in the SANS Q range and a MaxEnt size distribution fit in the USANS Qrange for the $Ca(OH)_2$ component. **c**, Predicted SANS/USANS data for OPC in D_2O and predicted USAXS data for OPC in H_2O, based on rescaling the C–S–H and $Ca(OH)_2$ components using SAXS and SANS scattering contrasts derived from our final results. Measured data in the SANS and USAXS ranges are shown for comparison. The inset shows the MaxEnt size distribution for the micrometre-scale $Ca(OH)_2$ component.

is broadly consistent with that derived earlier from SANS contrast measurements. The C–S–H and $Ca(OH)_2$ components can also be reassembled to predict the observed SANS for OPC in D_2O and the observed SAXS for OPC in H_2O. Figure 5c indicates that such predictions closely match the measured data. Addition of low-Q USANS data also enables the micrometre-scale $Ca(OH)_2$ microstructure to be distinguished from the nanoscale $Ca(OH)_2$. The micrometre-scale crystallite size distribution can be quantified by applying the maximum-entropy size distribution algorithm, MaxEnt[42], to the data in the USANS low-Q range (see Fig. 5c, inset). (See Supplementary Information for further discussion.)

By applying fundamental principles to a combination of scattering studies, we have established a representative mass density and H_2O mass fraction within the solid phase of C–S–H gel that forms between the clinker grains as the main binding phase in calcium-silicate-based cements. For cements where the C–S–H Ca/Si ratio is 1.7, we have established a C–S–H formula: $(CaO)_{1.70}(SiO_2)(H_2O)_{1.80}$ with a mass density of 2.604(22) $Mg\,m^{-3}$ and a water mass fraction of 0.174(4). These data differ from those of so-called D-dried[2] C–S–H, where around 1.4 $H_2O\,mol^{-1}$ is incorporated into the solid structure, implying that D-drying removes 0.4 $H_2O\,mol^{-1}$ from within the C–S–H particles. Conversely, our solid C–S–H phase contains 0.3 $H_2O\,mol^{-1}$ less than C–S–H dried to 11% RH (2.1 $H_2O\,mol^{-1}$), implying that 11% RH drying leaves 0.3 $H_2O\,mol^{-1}$ adsorbed on the C–S–H particle surface that is not part of the solid structure (Fig. 1).

The formula and mass density of C–S–H define the true solid/pore interface for C–S–H gel and the intrinsic SAXS and SANS contrasts ($|\rho_{CSH} - \rho_{H_2O}|^2$, and so on) that are critical for determining C–S–H volume fractions and surface areas from calibrated SAXS/SANS data. Although necessitating adjustments to previous results, the present study establishes a firmer basis for the quantitative characterization and modelling of C–S–H gel, provided that the nanoscale $Ca(OH)_2$, coexisting with the fractal C–S–H structure, is quantified. In a characterization of $Ca(OH)_2$ in hydrating cement that includes its nanoscale structure as well as its micrometre-scale size distribution, we have established that nanoscale $Ca(OH)_2$ contributes a fraction to the total surface area of 0.066(10) for OPC, 0.038(10) for C_3S and less in blended cements where $Ca(OH)_2$ is consumed. Generic studies of selected cements should enable nanoscale $Ca(OH)_2$ amounts to be deduced more generally as a function of hydration. The present results provide a foundation for such studies, not only of C–S–H gel but

also of other complex multicomponent gel systems, together with the appropriate molecular models[43].

In summary, we note that cement has a commercial and social importance unmatched by any other material except for silicon or steel. The structure is remarkably complex and one of the fundamental questions is how its C–S–H gel microstructure can retain such a fine particle size and high surface area for centuries while the solid is in contact with an aggressive liquid (water at pH 13). To answer this question, knowledge of the C–S–H formula and mass density, together with its water mass fraction and location, are essential. In this paper, we have presented values for these quantities, obtained for the first time without recourse to drying methods that can affect the results. The insights gained into cement structure at the nanoscale level from such measurements may ultimately contribute to improvements in concrete durability that could save hundreds of millions of dollars in annual maintenance and repair costs for concrete structures.

METHODS

Cements were mixed with a 0.4 w/c mass ratio, hydrated for 28 d in H_2O at 20 °C and sliced into thin coupons of thickness ≈0.5 mm for USAXS, SANS and USANS. For SANS contrast variation, coupons were submerged in the appropriate H_2O/D_2O fluid mixture for 24 h before measurement, having first been measured in H_2O as a control. For methanol experiments, 28 d coupons were first submerged in CH_3OH for several days and then submerged for 24 h in the appropriate CH_3OH/CD_3OH fluid mix before measurement. All specimens were sealed in cells under saturated conditions with respect to the pore fluid.

SANS measurements were carried out at the NIST Center for Neutron Research (NCNR), Gaithersburg, MD, using the NIST/NSF NG3 SANS instrument[44] and the BT5 NSF USANS instrument[45]. The SANS neutron wavelength, λ, was 0.8 nm and three different instrument configurations were used to obtain data over the widest possible Q range of $0.05\,\mathrm{nm}^{-1} < Q < 3\,\mathrm{nm}^{-1}$. Data were recorded on a two-dimensional detector, corrected for detector sensitivity, electronic and parasitic background effects and sample absorption, then calibrated against the incident beam flux and normalized to unit sample volume. Finally, data were circularly averaged to obtain the absolute scattering cross-section (intensity). The USANS instrument, which exploits Bonse-Hart Si(220) crystal diffraction optics with $\lambda = 0.24$ nm, was used to extend the minimum Q down to $0.0003\,\mathrm{nm}^{-1}$. USANS data were corrected using an empty beam (blank) subtraction, calibrated with respect to the incident beam, and de-smeared to remove slit-smearing effects. The SANS and USANS data for each specimen were intercalated and normalized with respect to each other, producing in each case a single data set of the scattering cross-section, $\mathrm{d}\Sigma/\mathrm{d}\Omega$ or $I(Q)$, versus Q.

USAXS measurements were carried out on the NIST-built USAXS instrument[46] at UNICAT sector 33-ID at the Advanced Photon Source, Argonne National Laboratory, Argonne, Illinois. This instrument uses Bonse-Hart Si(111) optics and the X-ray energy used here was 11 keV ($\lambda = 0.113$ nm). USAXS data were corrected, calibrated and de-smeared in a similar manner to the USANS data, to give USAXS $I(Q)$ versus Q over the range $0.0015\,\mathrm{nm}^{-1} < Q < 1.8\,\mathrm{nm}^{-1}$.

Received 17 August 2006; accepted 13 February 2007; published 25 March 2007.

References

1. Le Chatelier, H. L. *Experimental Researches on the Constitution of Hydraulic Mortars* (McGraw, New York, 1905).
2. Taylor, H. F. W. *Cement Chemistry* 2nd edn (Thomas Telford, London, 1997).
3. Acker, P. in *Creep, Shrinkage, and Durability Mechanics of Concrete and Other Quasi-Brittle Materials* (eds Ulm, F. J., Bazant, Z. P. & Wittmann, F. H.) (Elsevier Science, New York, 2001).
4. Scherer, G. W. Structure and properties of gels. *Cement Concrete Res.* **29**, 1149–1157 (1999).
5. Pijaudier-Cabot, G., Gerard, B. & Acker, P. (eds) in *Proc. 7th Int. Conf. on Creep, Shrinkage, and Durability of Concrete and Concrete Structures* (Hermes Science, London, 2005).
6. Bazant, Z., Cusatis, G. & Cedolin, L. Temperature effect on concrete creep modeled by microprestress-solidification theory. *J. Eng. Mech.* **130**, 691–699 (2004).
7. Richardson, I. G. The nature of C–S–H in hardened cement pastes. *Cement Concrete Res.* **29**, 1131–1147 (1999).
8. Gaboriaud, F., Nonat, A., Chaumont, D., Craievich, A. & Hanquet, B. Si-29 NMR and small-angle X-ray scattering studies of the effect of alkaline ions (Li+, Na+, and K+) in silico-alkaline sols. *J. Phys. Chem. B* **103**, 2091–2099 (1999).
9. Papavassiliou, G. *et al.* Role of the surface morphology in cement gel growth dynamics: A combined nuclear magnetic resonance and atomic force microscopy study. *J. Appl. Phys.* **82**, 449–452 (1997).
10. Cong, X. & Kirkpatrick, R. J. ^{29}Si MAS NMR study of the structure of calcium silicate hydrate. *Adv. Cement Based Mater.* **3**, 144–156 (1994).
11. Winslow, D. N. & Diamond, S. Specific surface of hardened cement paste as determined by small-angle X-ray scattering. *J. Am. Ceram. Soc.* **57**, 193–197 (1974).
12. Volkl, J. J., Beddoe, R. E. & Setzer, M. J. The specific surface of hardened cement paste by small-angle X-ray-scattering effect of moisture-content and chlorides. *Cement Concrete Res.* **17**, 81–88 (1987).
13. Yang, R. H., Liu, B. Y. & Wu, Z. W. Study on the pore structure of hardened cement paste by SAXS. *Cement Concrete Res.* **20**, 385–393 (1990).
14. Winslow, D., Bukowski, J. M. & Young, J. F. The early evolution of the surface of hydrating cement. *Cement Concrete Res.* **24**, 1025–1032 (1994).
15. Beddoe, R. E. & Lang, K. Effect of moisture on fractal dimension and specific surface of hardened cement paste by small-angle X-ray-scattering. *Cement Concrete Res.* **24**, 605–612 (1994).
16. Winslow, D., Bukowski, J. M. & Young, J. F. The fractal arrangement of hydrated cement paste. *Cement Concrete Res.* **25**, 147–156 (1995).
17. Thomas, J. J., Jennings, H. M. & Allen, A. J. The surface area of hardened cement paste as measured by various techniques. *Concrete Sci. Eng.* **1**, 45–64 (1999).
18. Vollet, D. R. & Craievich, A. F. Effects of temperature and of the addition of accelerating and retarding agents on the kinetics of hydration of tricalcium silicate. *J. Phys. Chem. B* **104**, 12143–12148 (2000).
19. Allen, A. J. *et al.* A small-angle scattering study of cement porosities. *J. Phys. D* **15**, 1817–1833 (1982).
20. Pearson, D., Allen, A. J., Windsor, C. G., Alford, N. McN. & Double, D. D. An investigation on the nature of porosity in hardened cement pastes using small-angle neutron scattering. *J. Mater. Sci.* **18**, 430–438 (1983).
21. Pearson, D. & Allen, A. J. A study of ultrafine porosity in hydrated cements using small-angle neutron scattering. *J. Mater. Sci.* **20**, 303–315 (1985).
22. Allen, A. J., Oberthur, R. C., Pearson, D., Schofield, P. & Wilding, C. R. Development of the fine porosity and gel structure of hydrating cement systems. *Phil. Mag. B* **56**, 263–288 (1987).
23. Haussler, F., Eichhorn, F., Rohling, S. & Baumbach, H. Monitoring of the hydration process of hardening cement pastes by small-angle neutron scattering. *Cement Concrete Res.* **20**, 644–654 (1990).
24. Castano, V. M., Schmidt, P. W. & Hornis, H. G. Small-angle scattering studies of the pore structure of polymer-modified portland cement pastes. *J. Mater. Res.* **5**, 1281–1284 (1990).
25. Allen, A. J. Time-resolved phenomena in cements, clays and porous rocks. *J. Appl. Cryst.* **24**, 624–634 (1991).
26. Eichhorn, F., Haussler, F. & Baumbach, H. Structural studies on hydrating cement pastes. *J. Phys. IV* **3**, 369–372 (1993).
27. Adenot, F., Auvray, L. & Touray, J. C. Determination of the fractal dimension of CSH aggregates (hydrated calcium silicates) of different origins and compositions —consequences for studies of cement paste durability. *C. R. Acad. Sci. II* **317**, 185–189 (1993).
28. Janik, J. A., Kurdowski, W., Podsiadly, R. & Samseth, J. Studies of fractal aspects of cement. *Acta Phys. Pol. A* **90**, 1179–1184 (1996).
29. Haussler, F., Hempel, M. & Baumbach, H. Long-time monitoring of the microstructural change in hardening cement paste by SANS. *Adv. Cement Res.* **9**, 139–147 (1997).
30. Allen, A. J. & Livingston, R. A. Relationship between differences in silica fume additives and fine scale microstructural evolution in cement based materials. *Adv. Cement Based Mater.* **8**, 118–131 (1998).
31. Thomas, J. J., Jennings, H. M. & Allen, A. J. The surface area of cement paste as measured by neutron scattering —evidence for two C–S–H morphologies. *Cement Concrete Res.* **28**, 897–905 (1998).
32. Heinemann, A. *et al.* Fractal microstructures in hydrating cement paste. *J. Mater. Sci. Lett.* **18**, 1413–1416 (1999).
33. Heinemann, A., Hermann, H. & Haussler, F. SANS analysis of fractal microstructures in hydrating cement paste. *Physica B* **276**, 892–893 (2000).
34. Thomas, J. J., Chen, J. J., Allen, A. J. & Jennings, H. M. Effects of decalcification on the microstructure and surface area of cement and tricalcium silicate pastes. *Cement Concrete Res.* **34**, 2297–2307 (2004).
35. Thomas, J. J., Jennings, H. M. & Allen, A. J. Determination of the neutron scattering contrast of hydrated portland cement paste using H_2O/D_2O exchange. *Adv. Cement Based Mater.* **7**, 119–122 (1998).
36. Richardson, I. G. Tobermorite/jennite- and tobermorite/calcium hydroxide-based models for the structure of C–S–H: Applicability to hardened pastes of tricalcium silicate, beta-dicalcium silicate, portland cement, and blends of portland cement with blast-fumace slag, metakaolin, or silica fume. *Cement Concrete Res.* **34**, 1733–1777 (2004).
37. Porod, G. in *Small-Angle X-ray Scattering* (eds Glatter, O. & Kratky, O.) (Academic, London, 1982).
38. Sears, V. F. Neutron scattering lengths and cross sections. *Neutron News* **3.3**, 29–37 (1992).
39. Allison, S. K., Fox, J. P., Hargreaves, R. & Bates, S. P. Clustering and microimmiscibility in alcohol-water mixtures: Evidence from molecular-dynamics simulations. *Phys. Rev. B* **71**, 024201 (2005).
40. Chantler, C. T. *et al.* X-ray form factor, attenuation and scattering tables (version 2. 1). (National Institute of Standards and Technology, Gaithersburg, 2005) Available online at: http://physics.nist.gov/ffast.
41. Brouwers, H. J. H. The work of Powers and Brownyard revisited: Part 1. *Cement Concrete Res.* **34**, 1697–1716 (2004); *ibid* Part 2 *Cement Concrete Res.* **35,** 1922–1936 (2005).
42. Potton, J. A., Daniell, G. J. & Rainford, B. D. Particle-size distributions from SANS data using the maximum-entropy method. *J. Appl. Cryst.* **21**, 663–668 (1988).
43. Kirkpatrick, R. J., Kalinichev, A. G., Hou, X. & Struble, L. Experimental and molecular dynamics modeling studies of interlayer swelling: Water incorporation in kanemite and ASR gel. *Mater. Struct.* **38**, 449–458 (2005).
44. Glinka, C. J. *et al.* The 30 m small-angle neutron scattering instruments at the National Institute of Standards and Technology. *J. Appl. Cryst.* **31**, 430–445 (1998).
45. Barker, J. G. *et al.* Design and performance of a thermal-neutron double-crystal diffractometer for USANS at NIST. *J. Appl. Cryst.* **38**, 1004–1011 (2005).
46. Ilavsky, J., Jemian, P. R., Allen, A. J. & Long, G. G. Versatile USAXS (Bonse-Hart) facility for advanced materials research. *AIP Conf. Proc.* **705**, 510–513 (2004).

Acknowledgements

Thanks to C. Glinka, B. Hammouda, J. Barker, J. Ilavsky, P. R. Jemian and R. A. Livingston for scientific/technical support. Research at Northwestern University was supported by NSF grant CMS-0409571. SANS measurements are partly based on activities supported by NSF agreement DMR-9122444. The Advanced Photon Source is supported by US DoE, Office of Science contract W-31-109-ENG-38.

Correspondence and requests for materials should be addressed to A.J.A.

Supplementary Information accompanies this paper on www.nature.com/naturematerials.

Competing financial interests

The authors declare no competing financial interests.